

# Aero-Optical Measurements of a Mach 8 Boundary Layer

Kyle P. Lynch,\* Nathan E. Miller,† and Daniel R. Guildenbecher‡  
Sandia National Laboratories, Albuquerque, New Mexico 87123

and

Luke Butler§ and Stanislav Gordeyev¶  
University of Notre Dame, Notre Dame, Indiana 46545

<https://doi.org/10.2514/1.J062363>

Measurements are presented of the aero-optic distortion produced by a Mach 8 turbulent boundary layer in the Sandia Hypersonic Wind Tunnel. Flat optical windows installed in conformed test section walls enabled a double-pass arrangement of a collimated laser beam. The distortion of this beam was imaged by a high-speed Shack–Hartmann sensor using variable aperture sizes at a sampling rate of up to 1.75 MHz. Analysis is performed using two processing methods to extract the aero-optic distortion from the data: 1) a stitching method is applied to extract wavefronts without bias from a limited aperture size, and 2) a novel de-aliasing algorithm is proposed to extract convective-only deflection angle spectra and is demonstrated to correctly quantify the physical spectra even for relatively low sampling rates. Measurements of speed and size of large-scale convecting aero-optical structures are also presented. Overall levels of aero-optic distortions were estimated, and the results are compared with an existing theoretical model. It is shown that this model underpredicts the measured distortions regardless of the processing method used. Possible explanations for this discrepancy are presented. Finally, levels of the global streamwise jitter were estimated for different aperture sizes and compared with the results for the subsonic boundary layer. The results represent to-date the highest Mach number for which aero-optic boundary-layer distortion measurements are available.

## Nomenclature

$A$	=	piston coefficient
$C_f$	=	skin-friction coefficient
$F$	=	aero-optical scaling function
$f$	=	frequency, Hz
$f_l$	=	focal length, m
$f_s$	=	sampling frequency, Hz
$G_A$	=	aperture transfer function
$K_{GD}$	=	Gladstone–Dale constant, m <sup>3</sup> /kg
$k$	=	wavenumber, 1/m
$M$	=	Mach number
$N$	=	number of points
$n$	=	index of refraction
$OPD$	=	optical path difference, m
$P$	=	pressure, Pa
$R$	=	two-point correlation function
$Re$	=	Reynolds number
$St$	=	Strouhal number
$S_W$	=	wavefront autospectral density function, m <sup>2</sup> /Hz
$S_\theta$	=	deflection-angle autospectral density function, rad <sup>2</sup> /Hz
$T$	=	temperature, K
$t$	=	time, s
$U$	=	velocity, m/s

$W$	=	wavefront, m
$x, y, z$	=	spatial positions, m
$\delta$	=	boundary-layer thickness, m
$\theta$	=	deflection angle, rad
$\theta_G, \theta_{G,z}$	=	tip/tilt plane fit coefficients
$\rho$	=	density, kg/m <sup>3</sup>

## Subscripts

$Ap$	=	aperture
$c$	=	convective
$G$	=	global
$HOT$	=	high-order terms
$rms$	=	root-mean-square
$0$	=	stagnation conditions
$\infty$	=	freestream conditions

## I. Introduction

AERO-OPTICAL distortions are caused by the dependence of the index of refraction,  $n$ , on the gas density  $\rho$ . This is described by the Gladstone–Dale relation,  $n - 1 = \rho K_{GD}$ , where  $K_{GD}$  is the Gladstone–Dale constant. This constant depends on the gas mixture and wavelength. For air at visible wavelengths,  $K_{GD} \approx 2.27 \times 10^{-4}$  m<sup>3</sup>/kg [1]. Light passing through a region of flow with varying density will therefore be distorted due to the varying index of refraction field. This distortion is typically quantified by the optical path difference ( $OPD$ ), defined as the line-of-sight integral of the fluctuating index of refraction:

$$OPD(x, y, t) = \int n'(x, y, z, t) dz = K_{GD} \int \rho'(x, y, z, t) dz \quad (1)$$

Knowledge of the  $OPD$  and its statistical properties is required to estimate imaging quality, focusing performance, or far-field beam quality when light passes through a region of variable density [2]. Measurement of the  $OPD$  is also required for developing adaptive optics to improve performances of optical systems [3]. This paper illustrates methods to measure both the  $OPD$  and the related quantity of optical jitter in a hypersonic boundary layer that can be used for these purposes.

Received 22 August 2022; revision received 10 October 2022; accepted for publication 18 October 2022; published online 30 November 2022. Copyright © 2022 by the American Institute of Aeronautics and Astronautics, Inc. The U.S. Government has a royalty-free license to exercise all rights for Governmental purposes. All other rights are reserved by the copyright owner. All requests for copying and permission to reprint should be submitted to CCC at [www.copyright.com](http://www.copyright.com); employ the eISSN 1533-385X to initiate your request. See also AIAA Rights and Permissions [www.aiaa.org/randp](http://www.aiaa.org/randp).

\*Senior Member of Technical Staff, Aerosciences Department; klynch@sandia.gov. Senior Member AIAA (Corresponding Author).

†Senior Member of Technical Staff, Aerosciences Department. Member AIAA.

‡Distinguished Member of Technical Staff, Diagnostic Science and Engineering Department. Associate Fellow AIAA.

§Graduate Student, Department of Aerospace and Mechanical Engineering. Member AIAA.

¶Associate Professor, Department of Aerospace and Mechanical Engineering. Associate Fellow AIAA.

We would also like to mention that the wavefront  $W$  of the collimated beam can be very closely approximated as a negative value of the  $OPD$ :  $W(x, y, t) = -OPD(x, y, t)$  [4]. Since the negative sign does not affect statistics of the wavefronts, such as  $OPD_{rms}$  and spectra, for simplicity we will refer to  $OPD$  as a wavefront.

The aero-optical phenomena occurring in subsonic and low-supersonic flows are well established [4]; however, there are fewer studies quantifying these phenomena at hypersonic speeds. Wyckham and Smits [5] performed measurements at transonic speeds and at approximately Mach 7.7 using a two-dimensional (2-D) wavefront sensor. They showed that large-scale motions on the order of the boundary-layer thickness dominated the measured distortions and proposed a wavefront distortion scaling based on bulk flow parameters. Subsequently, Gordeyev et al. [6] proposed a double-pass measurement for subsonic boundary layers and were able to measure convective speeds of aero-optic structures, deflection angle spectra, and the root mean square optical path difference  $OPD_{rms}$ . Using the strong Reynolds analogy (SRA), Gordeyev et al. [6,7] further proposed an analytical model to predict these aero-optical distortions and demonstrated that the model adequately predicts the observed values of  $OPD_{rms}$ . These techniques were extended to Mach 3.0 and 4.3 by Gordeyev et al. [8], and to the hypersonic regime in the Boeing/AFOSR Mach 6 Quiet Tunnel by Gordeyev and Juliano [9,10]. The latter showed that the measured  $OPD_{rms}$  values become consistently larger than predicted by the existing model for lower speed flat-plate turbulent boundary layers. Further, they conjectured that the assumptions underlying this model, originally developed for subsonic and low-supersonic boundary layers, become increasingly invalid in the hypersonic regime.

Several other experimental hypersonic aero-optic studies exist in the literature, but do not explicitly quantify the distortions caused by the boundary layer. In Winter et al. [11], image distortion measurements were performed using image calibration targets, but quantitative wavefront measurements were not performed. Lee et al. [12] performed experiments in a reflected shock tunnel with an internally mounted wavefront sensor in a wedge model. Mean tilt, boresight error, and Strehl ratio were measured, but the  $OPD_{rms}$  distortion was not reported.

The objective of this work is to extend the measurements performed in [9] to a higher Mach number and use these measurements to evaluate the efficacy of an existing aero-optics model. In Sec. II, the experimental setup and flow conditions are detailed. In Sec. III, a description of the data reduction procedures is given. In Sec. IV, the aero-optics results are reported, compared to the model, and a discussion is presented over the findings.

## II. Experimental Campaign

### A. Wind Tunnel Facility

The Sandia Hypersonic Wind Tunnel (HWT) is a blowdown-to-vacuum facility with interchangeable nozzles for Mach 5, 8, or 14 operations. Typical runtimes are on the order of 30 s. The Mach 8 capability is used for all tests herein. It uses high-pressure nitrogen as a test gas, with a stagnation pressure  $P_0$  and temperature  $T_0$  range from 1.7 to 6.9 MPa and 500 to 890 K, respectively. The test section is circular with a diameter of 35.6 cm. The freestream noise levels have been previously estimated between 3 and 5% using Pitot pressure measurements [13]. The specific test conditions approximately match the Mach 7.9 case of Smith et al. [14], with  $P_0 = 4.7$  MPa and  $T_0 = 620$  K. Isentropic relations and Sutherland's law yield approximate freestream conditions  $T_\infty = 45$  K,  $\rho_\infty = 0.04$  kg/m<sup>3</sup>, and  $Re_\infty = 14.0 \times 10^6$ /m. A CFD simulation of this condition was used to estimate the boundary-layer thickness  $\delta = 40.6$  mm, skin friction coefficient  $C_f = 6.13 \times 10^{-4}$ , and freestream velocity  $U_\infty \approx 1100$  m/s. Several runs were performed for repeatability with multiple imaging configurations as shown in Table 1. The tunnel has limited closed-loop control, leading to slight variation in conditions between runs.

### B. Optical Configuration

Measurements were collected using a high-speed Shack–Hartmann wavefront sensor with a schematic shown in Fig. 1. A continuous wave (CW) laser source (Coherent Verdi) was launched into a fiber and brought to an optical table beside the wind tunnel. The output of the fiber was collimated to a diameter of 22.5 mm using a 250 mm achromat lens and, after passing through a 50/50 nonpolarizing beam-splitter cube, was directed into the test section. A pair of lenses, 150 and 500 mm, were used to expand the beam from 22.5 mm to the aperture diameter of 75 mm inside the test section. Two conformal tunnel wall inserts provided a smooth transition to a pair of flat 75 mm BK7 windows. The test section smoothly transitioned the circular test section to be tangent. The inserts also aligned the windows tangent to the nozzle contour, to remove an angle discontinuity that could lead to the formation of weak shock waves. These windows were the effective aperture of the system.

The beam was reflected by a 0 deg mirror after exiting the second insert and made a second pass through the test section along the same path. The beam was contracted using the same lens pair, reflected off the 50/50 beam splitter, and projected onto a custom microlens array (MLA; focal length = 38 mm, pitch = 0.3 mm). The focal spots of the MLA were imaged using a Phantom TMX7510 monochrome high-speed camera (18.5  $\mu$ m/pixel size). In this setup, the image plane of the camera and lens system was focused to the location of the 0 deg mirror. The spatial resolution of the system was measured using a dot card as 16.3 px/mm, which yielded a spatial resolution of the deflection angles of  $\Delta x = \Delta z = 1.0$  mm.

For runs 2 and 7, a different set of lenses (500 and 400 mm) were used to change the beam size in the test section, resulting in the enhanced spatial resolution of the measured deflection angles of  $\Delta x = \Delta z = 0.24$  mm. This resolution was verified by using the dot card, as described above.

Two imaging rates and fields of view were used to adequately capture convecting turbulence and the spatial characteristics of the aero-optically active flow structures. The first configuration used the full sensor size of  $1280 \times 800$  px at 76 kHz to measure the 2-D array of dots generated by the MLA. The second configuration cropped the camera sensor to  $1280 \times 32$  px to operate at the maximum frame rate of 1.75 MHz. This allowed two rows of lenslets to be imaged. The exposure time was set to 0.3  $\mu$ s, which ensured that blurring caused by convection occurred within approximately a single lenslet diameter. A summary of the imaging configurations and relevant experimental conditions are given in Table 1. For each imaging configuration, the sampling duration is approximately 1–3 s, which began after the tunnel reached stable flow conditions.

Image processing consists of time-series dot shift estimation using an intensity centroiding code. The time-averaged shifts were subtracted from the time series to remove stationary distortions. No image preprocessing or intensity corrections are performed. The shifts were then converted to deflection angles based on the geometry of the lenslet array.

## III. Data Reduction

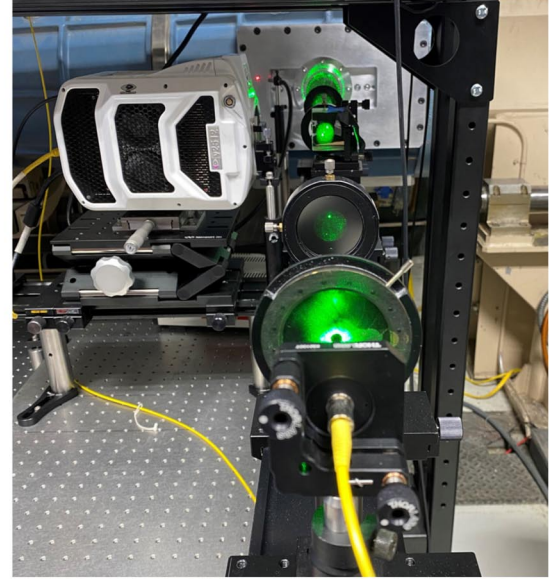
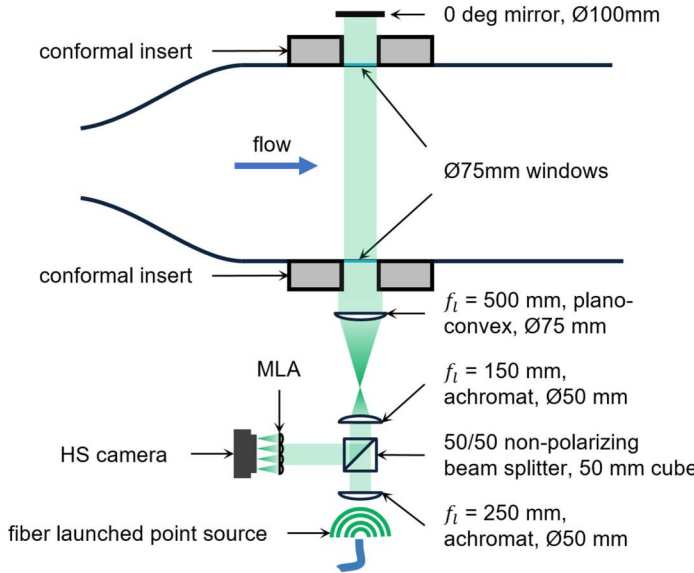
These experiments aimed to extract the time-averaged magnitude of aero-optic wavefront distortions  $OPD_{rms}$  and the corresponding convective speed  $U_c$  of the underlying aero-optically active flow structures in the hypersonic turbulent boundary layer. The Shack–Hartmann sensor measured deflection angles ( $\theta, \theta_z$ ) at discrete locations ( $x, z$ ) over the aperture. The deflection angles are related to the wavefront,  $OPD(x, z, t)$ , via the spatial gradient,  $\theta = (\partial OPD / \partial x)$ ,  $\theta_z = (\partial OPD / \partial z)$ . The deflection angles were integrated to obtain the 2-D wavefronts over the aperture using Southwell's method [15]. To make the solution unique, the spatial mean value of the wavefront (piston component) was forced to zero at each time,  $\int_{Ap} OPD(x, z, t) dx dz = 0$ . Two methods were used to extract wavefront statistics: first, a stitching method based on the wavefronts, and second, a spectral dispersion analysis on the deflection angles.

As shown in Fig. 1, the beam propagated through two boundary layers, one on each side of the tunnel. The approach of Gordeyev et al. [6,7] was adopted, which assumes that the boundary layers on

**Table 1** Parameters of dataset

Run	Frame rate, kHz	Record length, s	No. of lenslets	Physical aperture size, mm	Spatial resolution ( $\Delta x = \Delta z$ ), mm	$P_0$ , MPa	$T_0$ , K	$U_\infty$ , m/s <sup>a</sup>	$\rho_\infty$ , <sup>a</sup> kg/m <sup>3</sup>
2	1000.0	2.4	1 × 62	0.2 × 14.6	0.24	4.74 ± 0.03	617 ± 11	1089	0.037
7	396.226	1.7	5 × 64	1.0 × 15.1	0.24	4.75 ± 0.05	624 ± 12	1095	0.036
27	76.086	1.1	50 × 70	50.0 × 70.0	1.0	4.76 ± 0.03	625 ± 12	1098	0.037
29	76.086	1.1	50 × 70	50.0 × 70.0	1.0	4.76 ± 0.03	609 ± 12	1084	0.038
32	1750.0	1.1	2 × 70	2 × 70.0	1.0	4.85 ± 0.05	606 ± 12	1084	0.038

<sup>a</sup>Estimated from isentropic relations and  $P_0$  and  $T_0$  tunnel measurements.

**Fig. 1** Left: schematic optical configuration. Right: photograph of setup installed by the wind tunnel.

both sides are statistically identical and independent. Thus, the combined value of  $OPD_{\text{rms}}^2$  from two independent boundary layers is related to  $OPD_{\text{rms}}$  of a single boundary layer as

$$\begin{aligned}
 OPD_{\text{double,rms}}^2 &\equiv \overline{(OPD_1(t) + OPD_2(t))^2} \\
 &= \overline{(OPD_1(t))^2} + 2\overline{OPD_1(t) \cdot OPD_2(t)} \\
 &\quad + \overline{(OPD_2(t))^2} = OPD_{1,\text{rms}}^2 + OPD_{2,\text{rms}}^2 \\
 &= 2 \cdot OPD_{\text{rms}}^2
 \end{aligned}$$

Here the overbar denotes time-averaging. Therefore, the statistics of the single boundary layer were extracted from double boundary-layer measurements as  $OPD_{\text{rms}} = OPD_{\text{double,rms}}/\sqrt{2}$ .

#### A. Reconstruction via the Stitching Method

The 2-D wavefronts for runs 27 and 29 were measured over a finite size aperture. When an instantaneous piston component was removed from each wavefront, it reduced the resulting wavefront amplitude. The wavefront measurements were also corrupted by mechanical vibrations. These manifested as additional time-varying spatial tip/tilt components imposed on the measured wavefronts and were also removed from each snapshot of the wavefront. The definition of tip/tilt components and the removal procedure will be given later in Sec. IV.D. Their removal further reduces the overall level of measured aero-optical distortions. The removed piston and tip/tilt components depend on the aperture size; therefore, the residual (sometimes termed high-order)  $OPD_{\text{rms}}(\text{Aperture})$  is a function of the aperture size. This reduction is called the aperture effect in literature [6,16,17], and can be expressed in terms of the

aperture function,  $G_A(\text{Aperture}) = OPD_{\text{rms}}(\text{Aperture})/OPD_{\text{rms}}$ , where  $OPD_{\text{rms}}$  is the level of aero-optical distortions for sufficiently large apertures. Examples of turbulent boundary-layer aperture functions for different Mach numbers, extracted from one-dimensional (1-D) wavefront data, can be found in [9]. The aperture functions are similar for a wide range of Mach numbers, and are monotonically increasing functions, leveling off for apertures on the order of  $10\delta$ .

As mentioned before, the time-varying tip/tilt components were removed from each wavefront, as they were corrupted by mechanical vibrations. Yet, some portion of the removed tip/tilt is related to aero-optical effects. The stitching method allows for reintroducing the missing tip/tilt component to each wavefront [17,18]. The stitching method is schematically illustrated in Fig. 2. It invokes Taylor's frozen field hypothesis to assume that the underlying wavefront structure does not substantially change between the adjacent frames, but simply convects downstream. An example of two consecutive wavefronts is shown in Fig. 2a. The two wavefronts have the same structure, outlined by a dotted line, located at different spatial regions for each wavefront. If the wavefront at a later time is shifted properly in space, the outlined structure in the shifted wavefront will match the structure in the first wavefront in the overlapping region, as shown in Fig. 2b. Physically, the wavefront in the overlapping region should be approximately the same, as it is an integral of the density field. However, because different amounts of tip/tilt were removed from each wavefront, the tip/tilt-removed wavefront in the overlapping region will be different. By analyzing the difference between the overlapping regions in both wavefronts, the aero-optical portion of tip/tilt can be calculated and added back to each wavefront. In this manner, the aperture effect can be circumvented. Also, the wavefronts can be combined or "stitched" to obtain a longer wavefront, as

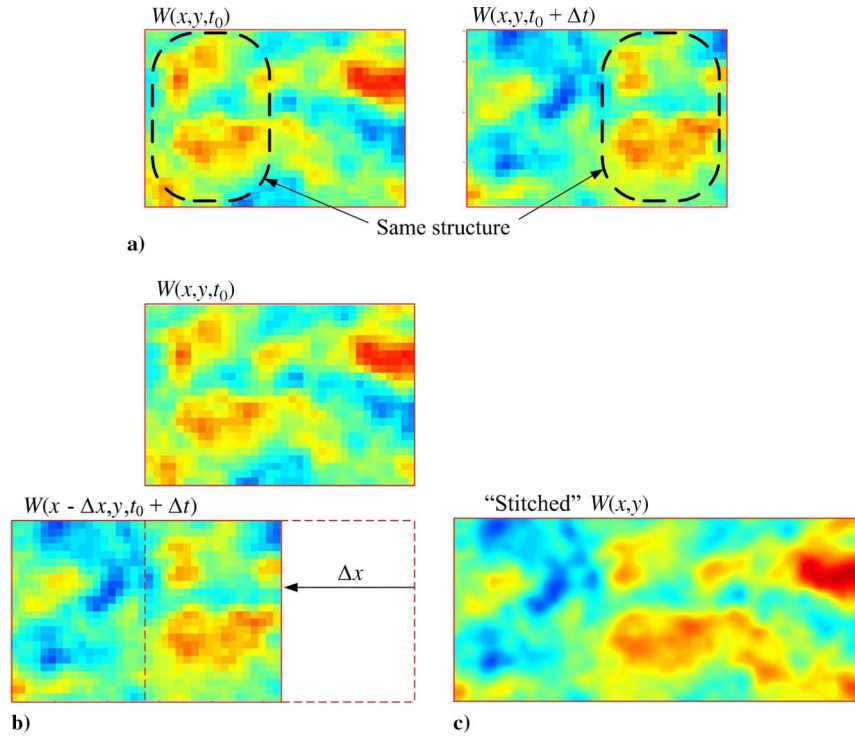


**Fig. 2** Schematic of the stitching method using actual measurement data. a) The two adjacent frames, separated by  $\Delta t$ , have common structures. b) The same two frames, with the latter shifted in space by  $\Delta x = -U_c \Delta t$ . c) The two frames are blended in the overlapping region forming a longer “stitched” wavefront. From [18].

demonstrated in Fig. 2c. The process is repeated along adjacent frames to produce a long streamwise strip of the wavefronts. This stitched wavefront contains only aero-optical distortions and is free of corruption from mechanical vibrations. A detailed description of the stitching method, the related uncertainty, and a comparison with experiments can be found in [17].

## B. Reconstruction Using Dispersion Analysis

An alternative to 2-D wavefront reconstruction is possible by operating the Shack–Hartmann sensor at a rate high enough to resolve the temporal derivative of the deflection angles. This rate is typically high enough where only a single row of lenslets can be acquired; therefore wavefront integration as detailed in the previous section cannot be performed. This alternative method again exploits the convection of aero-optical structures over the aperture. Taylor’s frozen field hypothesis allows approximation of the wavefront spatial derivatives via temporal derivatives,  $(\partial W / \partial x) = (1 / U_c)(\partial W / \partial t) = -\theta$  [6]. This is integrated in time since the time-series of the deflection angles and the convective speed were known. The Fourier transform yields  $(i\omega / U_c)\hat{W} = -\hat{\theta}$ , which provides a useful relation between the autospectral density functions of the wavefront,  $S_w(f)$ , and the streamwise deflection angle,  $S_\theta(f)$  [6]:

$$S_w(f) = \left( \frac{U_c}{2\pi f} \right)^2 S_\theta(f) \quad (2)$$

This spectral form is advantageous, as it allows filters to be applied for removal of vibrations, electronic noise, etc. The overall level of aero-optical distortions  $OPD_{\text{rms}}$  is calculated by integrating the deflection angle spectrum over frequency:

$$OPD_{\text{rms}}^2 = 2U_c^2 \int_0^\infty \frac{S_\theta(f)}{(2\pi f)^2} df \quad (3)$$

The integration bounds must only include the spectral content associated with the convecting structures. A dispersion analysis of these deflection angles [6,19] was effective for isolating these. This approach computed a 2-D autospectral density function of the

deflection angles  $S_\theta(f, k_x)$ , as described by Eq. (4). The spectrum was estimated using Welch’s method with no block overlap and squared-cosine block weighting following the procedure in Bendat and Piersol [20]. The block size was  $[N_t \times N_x]$  points, with  $N_t = 667,000$  temporal points,  $N_x = 67$  spatial points for run 2,  $N_t = 2,000,000$  temporal points,  $N_x = 62$  spatial points for run 7, and  $N_t = 1,000,000$  temporal points,  $N_x = 70$  spatial points for run 32.

$$\begin{aligned} \hat{\theta}(k_x, f) &= \int_0^D \int_0^T \theta(t, x) e^{-j2\pi(f t + k_x x)} dt dx, \\ S_\theta(f, k_x) &= \frac{\langle \hat{\theta}^*(k_x, f) \hat{\theta}(k_x, f) \rangle}{T \cdot \text{Ap}} \end{aligned} \quad (4)$$

Here  $T = N / f_s$  is the block duration,  $N$  is the block size,  $\text{Ap} = N_x \times \Delta x$  is the beam aperture in the streamwise direction, and angled brackets denote block averaging. The autospectral density functions for different sampling frequencies corresponding to different runs are shown in Fig. 3. The prominent band feature is caused by the convecting coherent structures; these appear as constant slope branches in the dispersion spectra defined by  $2\pi f t - k_x x = \text{const}$ , where the slope indicates the direction and magnitude of the convecting velocity as  $U_c = 2\pi f / k_x$ . Another feature of the spectra is severe aliasing, with additional branches appearing on both sides of the main branch. This spectral aliasing indicates that a direct implementation of Eq. (3) to compute  $OPD_{\text{rms}}$  will be biased, and it also hinders a two-point spectral cross-correlation technique to compute the convective speed [6].

To understand the origin of the spurious branches in Fig. 3, consider a purely convective signal. An idealized spectrum for a continuous 2-D Fourier transform (an infinite sampling frequency) is shown schematically in Fig. 4a as a single branch with a constant slope, determined by the convective speed. If the signal is sampled at a finite sampling frequency  $f_s$  and a finite spatial wavenumber  $k_{\text{max}}$ , the Nyquist–Shannon sampling theorem states that the resulting discrete spectrum will be a superposition of infinite number of continuous spectra, periodically shifted by  $[n \cdot f_s] \times [m \cdot k_{\text{max}}]$ , where  $n$  and  $m$  are integer numbers, as illustrated in Fig. 4b. If the original spectrum has frequency content above the Nyquist frequency



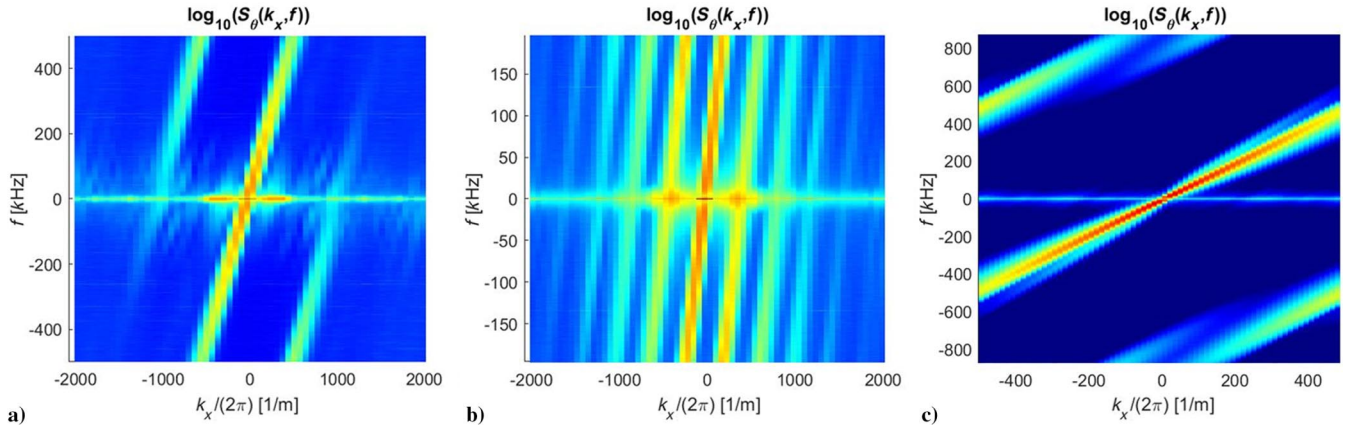


**Fig. 3** Two-dimensional spectra of the deflection angles for sampling frequency a)  $f_s = 1$  MHz,  $\Delta x = 0.24$  mm (run 2); b)  $f_s = 393$  kHz,  $\Delta x = 0.24$  mm (run 7); and c)  $f_s = 1.75$  MHz,  $\Delta x = 1$  mm (run 32). For (a) and (b), aliasing is predominantly in the frequency space. For (c), aliasing is present in both frequency and spatial wavenumber spaces.

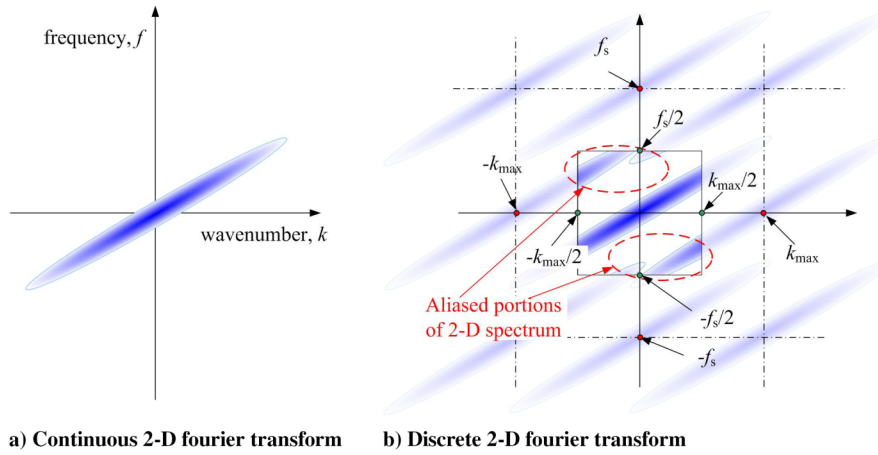


**Fig. 4** Schematic illustrating temporal aliasing of convective 2-D spectra with insufficient sampling frequency.

$f_s/2$  and above the spatial Nyquist wavenumber  $k_{\max}/2$ , it will result in shifted branches entering the range of frequencies–wavenumbers  $[-f_s/2, +f_s/2] \times [-k_{\max}/2, +k_{\max}/2]$ , as shown inside the rectangular box in Fig. 4a. This is a classic example of aliasing in discrete 2-D Fourier transforms.

Understanding the origin of the aliasing provides a possible way to remove it. The algorithm is demonstrated in Fig. 5. Consider a discrete 2-D spectrum, aliased in time and space, as in Fig. 3a. This can be shifted by  $\pm f_s, \pm 2f_s$ , and so on along the frequency axis, and shifted by  $\pm k_{\max}, \pm 2k_{\max}$  and so on along the wavenumber axis, to create a tiled spectrum, as in Fig. 5b. This leads to the main branch recovering its original shape. By applying a band filter, shown as a shaded region in Fig. 5c, the main branch can be isolated and

analyzed. Finally, the de-aliased temporal spectrum can be computed by integrating the band-passed 2-D spectrum in the wavenumber space:

$$S_\theta(f) = \frac{1}{2\pi} \int_{-\infty}^{\infty} \text{BandPass } S_\theta(f, k_x) dk_x \quad (5)$$

By slope fitting the ridge of the main branch, the convective speed  $U_c$  can also be computed and  $OPD_{\text{rms}}$  can be calculated from this de-aliased deflection angle spectrum by applying Eq. (3). This tiling approach has previously been used to extract the correct convective speeds and aero-optical levels in subsonic boundary layers [21].

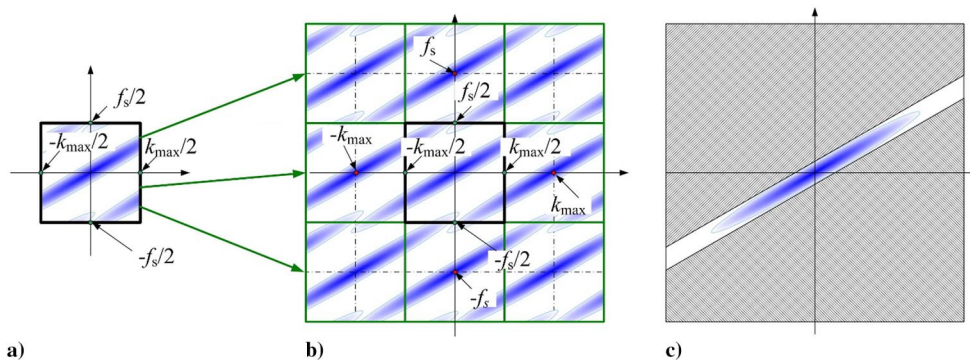


**Fig. 5** Schematic illustrating a proposed de-aliasing algorithm to recover the temporal spectrum.

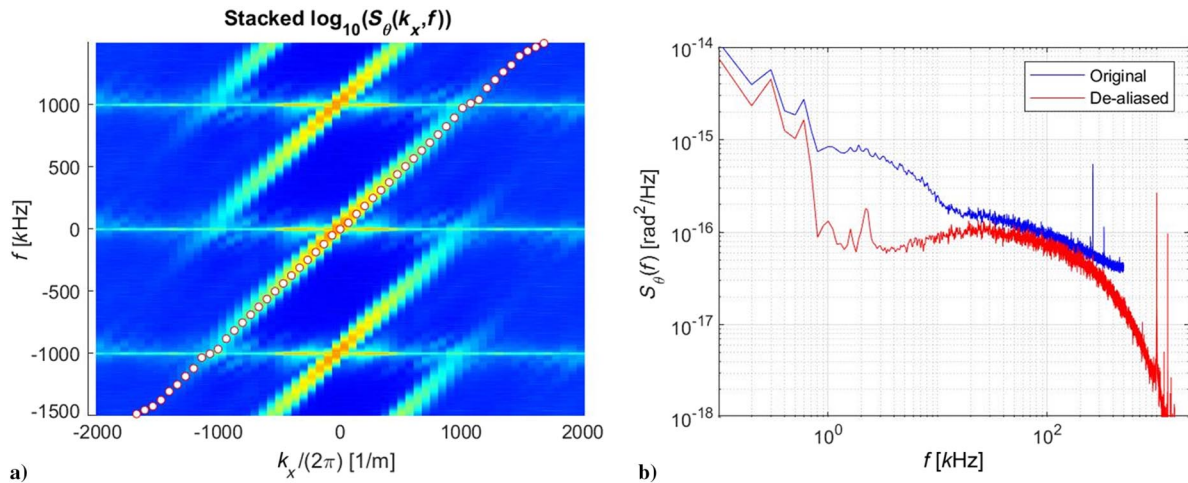
Implementation of the de-aliasing algorithm for the sampling frequency of 1 MHz and  $\Delta x = 0.24$  mm (run 2) is shown in Fig. 6. In this case, tiling the discrete spectrum only once, on top and on bottom, is sufficient to recover the main branch, as demonstrated in Fig. 6a. Open circles identify the ridge of the main branch, defined as the local spectrum intensity centroid [22], and a linear fit was used to compute the convective speed. Applying a band filter and integrating the spectrum in wavenumber space gives the de-aliased spectrum, shown as a red line in Fig. 6b. For comparison, the deflection angle spectrum from a single point is also plotted in Fig. 6b as a blue line. Contamination in the low-frequency range between 1 and 20 kHz is significantly reduced. More importantly, the de-aliased spectrum is extended up to 1.5 MHz, beyond the Nyquist frequency and even the sampling frequency. The sharp peaks at 1 and 2 MHz, which are multiples of the sampling frequency, are the artifacts of the incomplete removal of the zero-frequency component, evidenced by horizontal lines in Fig. 6a. The low end of the recovered spectrum below 1 kHz is still influenced by mechanical vibrations, which will be discussed in more details later in this paper.

Figure 7 demonstrates that the algorithm works well for a lower sampling frequency of 393 kHz (run 7). In this case, the discrete spectrum was tiled three times above and below to recover the original branch (see Fig. 7a). The de-aliased and single-point spectra are plotted in Fig. 7b. While the single-point spectrum is

significantly aliased over the whole range of the resolved frequencies, the de-aliased spectrum is similar to the de-aliased spectrum in Fig. 6b, and also extends well beyond the sampling frequency. As in Fig. 6, the sharp peaks at multiples of the sampling frequency are present in the recovered spectrum.

For run 32, the aliasing is present in both the frequency and wavenumber spaces, and the spectrum was tiled in both directions to fully recover the main branch. The result is shown in Fig. 8a. By applying a narrow filter to isolate the main branch from other branches, the spectrum was recovered and shown as a red line in Fig. 8b. The comparison with the original spectrum (blue line) revealed that the aliasing in this case is somewhat minimal as evidenced by small differences in both the low frequencies and close to the Nyquist frequency.

These examples demonstrate that if the imaging and lenslet setup have sufficient spatial resolution and number of spatial points, the corresponding deflection angle spectra can be recovered even for temporally/spatially undersampled data. Note that, at some values of the sampling frequency and spatial resolutions, for instance, for  $(f_s \Delta x / U_c) \approx 1$ , aliased components would tend to overlap, and the techniques presented here would fail [21]. Still, as demonstrated here, widely available high-speed cameras can readily provide sufficient temporal resolution for these measurements, and the proposed stacking method is recommended for eliminating the highest-frequency aliasing artifacts.



**Fig. 6** a) Stacked 2-D spectrum with the location of the main branch indicated with filled circles. b) The single-point and de-aliased temporal spectra of the deflection angles. The sampling frequency is  $f_s = 1$  MHz,  $\Delta x = 0.24$  mm (run 2).

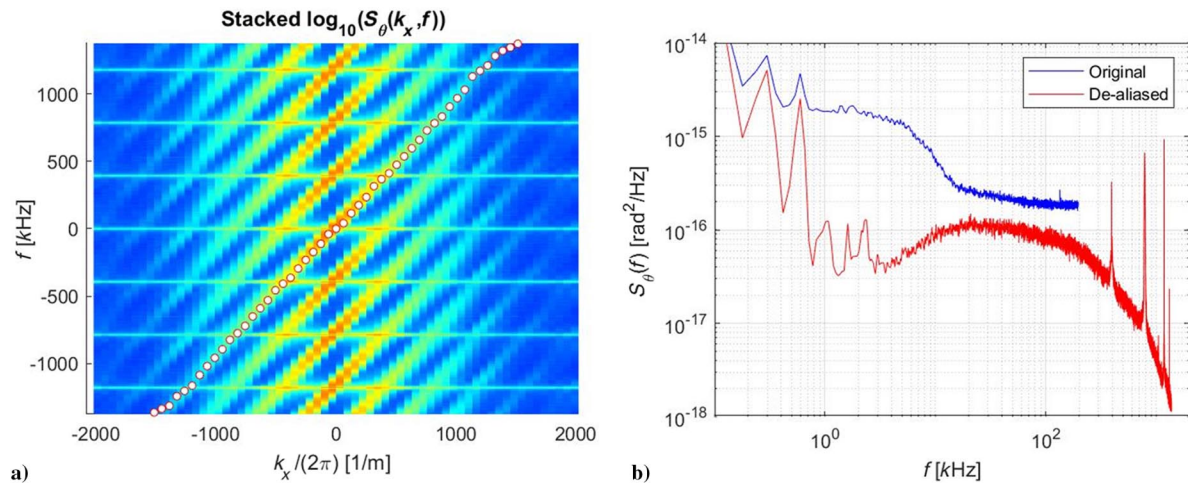


**Fig. 7** a) Stacked 2-D spectrum with the location of the main branch indicated with filled circles. b) The single-point and de-aliased temporal spectra of the deflection angles. The sampling frequency is  $f_s = 393$  kHz,  $\Delta x = 0.24$  mm (run 7).



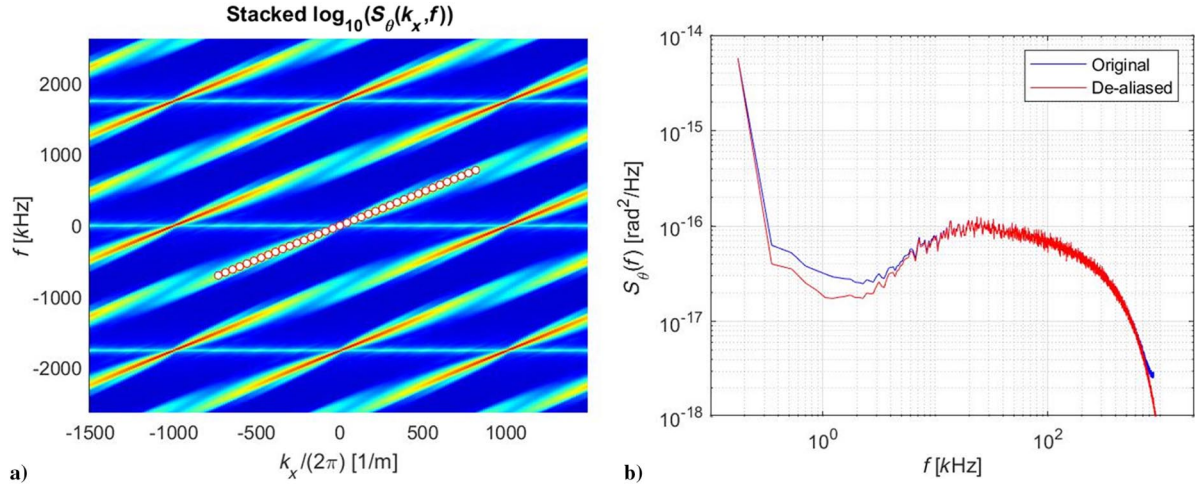


**Fig. 8** a) Stacked 2-D spectrum with the location of the main branch indicated with filled circles. b) The single-point and de-aliased temporal spectra of the deflection angles. The sampling frequency is  $f_s = 1.75$  MHz,  $\Delta x = 1$  mm (run 32).

## IV. Results and Discussion

### A. Analysis of Stitched Wavefronts

A small portion of the stitched wavefront for run 27 is shown in Fig. 9a. Note that, the original wavefront data were collected over the aperture of  $2\delta$  in the streamwise direction, while the full reconstructed wavefront extends over  $1400\delta$ . Aero-optical distortions from large-scale structures on the order of  $\sim 1\delta$  in the streamwise direction and  $\sim 0.5\delta$  in the spanwise direction can be clearly observed. The stitched long strip of the wavefronts was used to extract a large-aperture  $OPD_{rms}$  and two-point correlation function,  $R(\Delta x, \Delta z) = \langle OPD(x, z) OPD(x + \Delta x, z + \Delta z) \rangle_{(x,z)}$ , where the angled brackets denote spatial averaging. The normalized two-point correlation function,  $R(\Delta x, \Delta z)/R(\Delta x = 0, \Delta z = 0)$ , computed from the full stitched wavefront is shown in Fig. 9b. The OPD correlations are elongated in the streamwise direction,

with the correlations extending to about  $1.5\delta$  in the streamwise direction and approximately  $0.25\delta$  in the cross-stream direction. Interestingly, the correlation function is very similar to the correlation OPD function for subsonic boundary layers [23], including the presence of small negative correlations, centered at  $(\Delta x/\delta = \pm 1.5, \Delta z/\delta = \pm 0.5)$ . The similarity between the correlation functions indicates that the underlying large-scale structures for the subsonic and the hypersonic boundary layers are similar.

The long wavefront strip can also be used to extract the aero-optical levels for various apertures,  $OPD_{rms}(\text{Aperture})$ , and the aperture transfer function,  $G_A(\text{Aperture})$ . To do so, recall that the reconstructed wavefront is about  $1400\delta$  in the streamwise direction and  $Ap_z = 1.3\delta$  in the cross-stream direction. This long strip was broken into a set of wavefronts with a given streamwise aperture size,  $[\text{Aperture}, \text{Aperture}_z]$ . The cross-stream aperture,  $\text{Aperture}_z$ ,

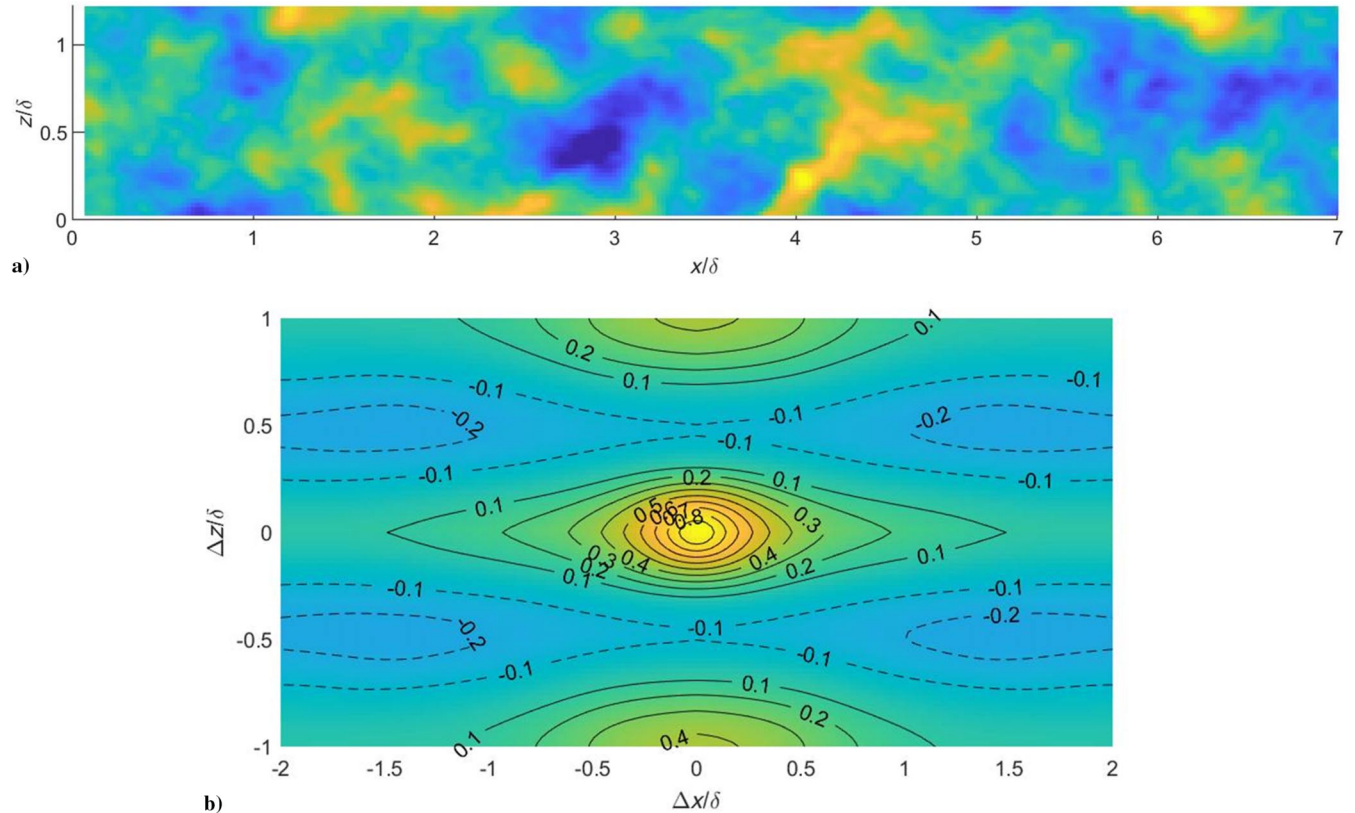


**Fig. 9** a) Stitched wavefront for run 27. b) Normalized two-point correlation function,  $R(\Delta x, \Delta z)/R(\Delta x = 0, \Delta z = 0)$ , for run 27.

was kept the same as for original wavefront set if  $\text{Aperture} > \text{Ap}_z$ , and as  $\text{Aperture}_z = \text{Aperture}$  if  $\text{Aperture} < \text{Ap}_z$ . After removing the piston and tip/tilt components from each wavefront (details will be discussed later in this paper), the residual  $OPD_{\text{rms}}(\text{Aperture})$  and the aperture transfer function,  $G_A(\text{Aperture})$ , were calculated.  $G_A(\text{Aperture})$  is plotted in Fig. 10. The aperture transfer functions extracted from turbulent boundary layers at other Mach numbers are also plotted for comparison. As expected, the aero-optical levels monotonically increase with the streamwise aperture size and approach a constant value for apertures larger than  $10\delta$ . The transfer function for the presented data is consistently higher than the transfer functions for lower Mach numbers. One reason for this is that the current transfer function was calculated using 2-D wavefront data, while the transfer functions for lower Mach numbers were estimated using 1-D wavefront data. Therefore, the 1-D transfer functions do not include any aero-optical distortions in the cross-stream direction and most likely underestimate the aero-optical distortions at smaller apertures.

### B. Deflection Angle Spectra and Convection Velocity

Comparison of de-aliased deflection angle spectra for different runs is presented in Fig. 11a. The results agree with each other well, demonstrating that the proposed tiling approach correctly extracts the deflection angle spectra even for severely undersampled cases, like run 7, where the sampling frequency was  $f_s = 393$  kHz. Small discrepancies can be observed at low frequencies below 10 kHz,

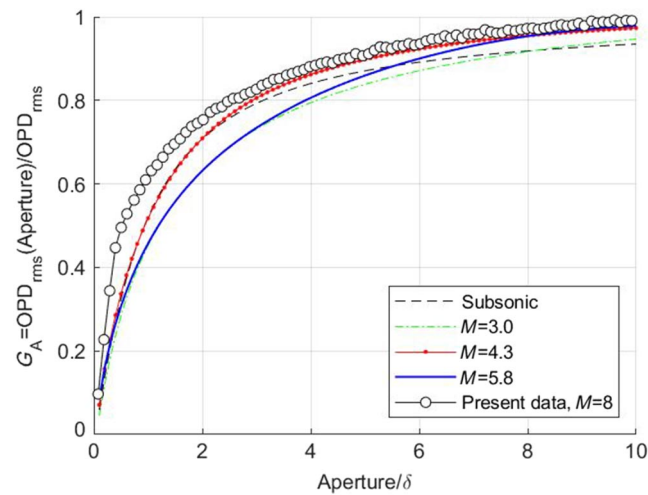


Fig. 10 The aperture transfer function,  $G_A(\text{Aperture})$ , calculated from the 2-D stitched wavefront. Aperture transfer functions at different Mach numbers from [6,9] are also plotted for comparison.

where different amounts of mechanical contamination from vibrating optical components are still present in the data. From Eq. (2) it follows that, for the wavefront spectrum to be finite at low frequencies, the deflection angle spectra should behave as  $\sim f^2$  in the low-frequency range. This expected spectral dependence is also plotted in Fig. 11a as a dashed line. All spectra deviate from this expected slope at low frequencies due to the presence of these contaminating vibration effects.

At higher frequencies above 500 kHz, the spectra for runs 2 and 7, while agreeing with each other, are consistently above the spectrum for run 32. Recall that runs 2 and 7 have a small spatial resolution of  $\Delta x = 0.24$  mm, while for run 32 the deflection angles were collected at larger  $\Delta x = 1$  mm. This discrepancy in spectra is attributed to the subaperture effects [6], when the deflection angles are averaged over the subaperture size, resulting in attenuation of the measured deflection angles at small scales (or, equivalently, high frequencies). In [6] it was demonstrated that the subaperture effects are significant for frequencies higher than  $f \gtrsim U_c/(\pi\Delta x)$ . For run 32, the subaperture attenuation frequency range starts at approximately 300 kHz, while for smaller subapertures of  $\Delta x = 0.24$  mm (runs 2 and 7) the attenuating range starts at much higher frequency of 1.2 MHz.

Figure 11b presents the de-aliased autospectral density function for the deflection angle versus normalized frequency,  $St_\delta = f\delta/U_\infty$ . Deflection angle spectra for  $M = 3, 4.3$ , and  $5.8$  from [9] are also plotted for comparison. Except for the vibration-corrupted low-frequency components, all spectra approximately collapse into each other for  $St_\delta > 0.3$ , indicating that the large-scale structure, which is responsible for most of the aero-optical distortions, does not change significantly with Mach number. The peak in all spectra is at approximately at  $St_\delta = 1$ , implying that the dominant aero-optically active structures are on the order of the boundary-layer thickness. This common spectral peak location over a wide range of Mach numbers, including the subsonic regime [6], is notable. This provides a non-intrusive method to estimate the turbulent boundary-layer thickness over a wide range of Mach numbers by sending a small-aperture laser beam normal to the boundary layer, measuring the resulting streamwise deflection angles, and finding the location of the peak in the deflection angle spectrum.

The convective speeds were extracted from the experimental data as described in Sec. III from dispersion analysis and the stitching method. The resulting convective speed was found to be approximately 950 m/s. The measurements of the convective speeds of aero-optical structures at lower Mach numbers [9] suggest that the convective speed should be approximately 0.95 of the freestream speed at  $M = 8$ . Thus, these measurements provide an estimate of the freestream speed of 1000 m/s. This value is slightly less than the freestream velocity of about 1090 m/s, estimated using isentropic relations, and less than the freestream velocity of 1100 m/s, estimated from perfect gas CFD simulations of the nozzle at similar stagnation

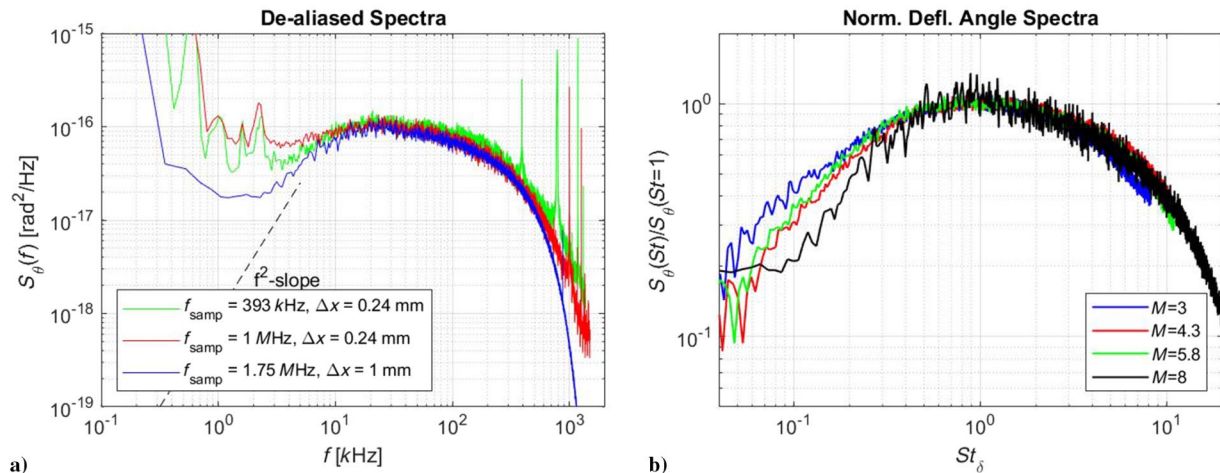


Fig. 11 a) Comparison of de-aliased deflection angle spectra for several runs. b) Deflection angle spectra as a function of  $St_\delta = f\delta/U_\infty$ , normalized by the value at  $St_\delta = 1$ . Black line: current data for  $M = 8$  ( $f_s = 1.75$  MHz,  $\Delta x = 1$  mm). Colored lines: data for  $M = 3, 4.3$ , and  $5.8$  from [9].



conditions. This overestimate of freestream velocity has been observed in other high-Mach-number tunnels and is attributed to the vibrational nonequilibrium of nitrogen throughout the expansion, which alters the state of the gas at the nozzle exit [24].

### C. Aero-Optical Levels and Comparison with a Theoretical Prediction

Both the stitched wavefronts and de-aliased deflection angle spectra were used to estimate the overall levels of aero-optical distortions  $OPD_{rms}$ . For the stitched wavefronts, the aperture was chosen to be  $10\delta$ , as it was determined to be a sufficiently large aperture to eliminate the aperture effect (see Fig. 10). As discussed before, the de-aliased deflection angle spectra are contaminated by the mechanical vibrations at low-frequency range. To correctly calculate  $OPD_{rms}$  values from the deflection angle spectra via Eq. (3), this low-frequency range should be removed from the data before the integration. Digital high-pass filters were implemented at cutoff frequencies of 3 kHz for runs 2 and 7 and of 2 kHz for run 32 to calculate  $OPD_{rms}$  values. The filters removed all spectral content below the cutoff values, including a contribution from any aero-optical effects in this frequency range. Thus, this approach tends to underestimate the  $OPD_{rms}$  values.

The theoretical model proposed in [6,7] states that

$$OPD_{rms} = F(M_\infty) K_{GD} \rho_\infty M_\infty^2 \delta (C_f)^{1/2} \quad (6)$$

where  $F(M_\infty)$  is only a function of the freestream Mach number. A comparison of the aero-optical distortion from the stitched wavefronts, de-aliased deflection angle spectra, and the theoretical model are shown in Fig. 12. The previous experimental results for other Mach numbers from [9] are also plotted for comparison. While the results from the deflection angles and the stitched wavefronts are close to each other,  $OPD_{rms}$  from the deflection angle spectra are consistently lower than  $OPD_{rms}$  values from the stitched wavefronts. This is an expected result, since application of high-pass filters to remove the vibration-contaminated lower range of the deflection angle spectra also removes aero-optical components present in this range, resulting in underestimating  $OPD_{rms}$  values.

The estimated  $OPD_{rms}$  are consistently higher, by a factor of two, than the model prediction. The normalized aero-optical distortions begin to plateau near a value  $F = 0.075$  for Mach numbers above 5. The deviation from the model prediction is expected, as assumptions such as the strong Reynolds analogy used to develop the model become increasingly invalid for  $M > 3$ . These assumptions are under investigation to extend the model to higher Mach numbers

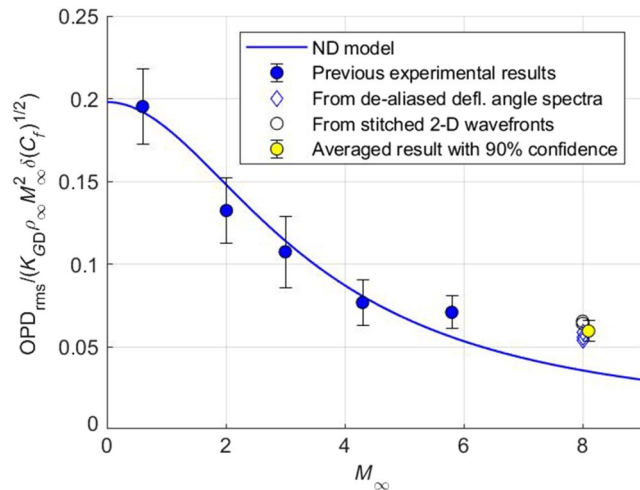


**Fig. 12** Normalized levels of  $OPD_{rms}$  computed using de-aliased deflection angle spectra and stitched wavefronts, and the averaged result with 90% confidence interval (shifted to the right for clarity). Normalized levels of  $OPD_{rms}$  at different Mach numbers from [9] and the theoretical model from [6,7] are plotted for comparison.

[25]. Also, other aero-optical sources, such as acoustic radiation from hypersonic turbulent boundary layers, might be responsible for higher than predicted values of  $OPD_{rms}$ .

### D. Estimate of Tip-Tilt Magnitude

In a typical analysis of wavefront data, spatiotemporally varying OPDs are decomposed into three components: a piston or a spatially uniform component,  $A(t)$ ; tip/tilt or linear components,  $\theta_G(t)$  and  $\theta_{G,z}$  in  $x$  and  $z$  directions; and a residual or a higher-order component,  $OPD_{HOT}(x, z, t)$ ,

$$OPD(x, z, t) = A(t) + \theta_G(t)x + \theta_{G,z}(t)z + OPD_{HOT}(x, z, t) \quad (7)$$

Subscript  $G$  in the linear components indicates that the linear components are defined over a full or a global aperture. All the components generally vary in time. The higher-order term results in distortions of the far-field intensity pattern, while the linear tilt components simply shift the far-field pattern in both  $x$  and  $z$  directions [17]. The piston mode does not affect the far-field pattern and is usually ignored in the analysis. Thus, in addition to distorting beam shapes or image focusing, aero-optical distortions can also change the overall optical pointing. These time-varying changes in pointing are also known as jitter.

To calculate tip/tilt components, typically a Zernike tilt (Z-tilt) definition [26] is used. To calculate Z-tilt, a least-squares fit is applied to the wavefronts by minimizing the following integral at every time step:

$$\int_{\text{Aperture}} (OPD(x, z, t) - A(t) - \theta_G(t)x - \theta_{G,z}(t)z)^2 dx dz \rightarrow \min \quad (8)$$

The resultant coefficients  $\theta_G(t)$ ,  $\theta_{G,z}(t)$ , and  $A(t)$  are the streamwise and the spanwise tilt, and the piston component, respectively. More information about explicit equations to compute these components are given in [17]. In a particular case of rectangular or round apertures, all these components can be computed as

$$\begin{aligned} \theta_G(t; \text{Aperture}) &= \frac{\int_{\text{Aperture}} x \cdot OPD(x, z, t) dx dz}{\int_{\text{Aperture}} x^2 dx dz}, \\ \theta_{G,z}(t; \text{Aperture}) &= \frac{\int_{\text{Aperture}} z \cdot OPD(x, z, t) dx dz}{\int_{\text{Aperture}} z^2 dx dz} \end{aligned} \quad (9)$$

$$A(t; \text{Aperture}) = \frac{\int_{\text{Aperture}} OPD(x, z, t) dx dz}{\int_{\text{Aperture}} dx dz} \quad (10)$$

Here it is explicitly recognized that the global tilt components and the piston mode depend on the aperture size and shape. These components were computed and removed from the apertured wavefronts, using the stitching method, to calculate the aperture transfer function for different aperture sizes presented in Fig. 10. The computed streamwise component of the global jitter was also used to compute the rms values for various apertures sizes,  $\theta_{G,rms}$  (Aperture).

When the aperture size goes to zero, the global streamwise tilt becomes the local streamwise deflection angle  $\theta(t)$ . In [17] it was shown that the root-mean square of the deflection angle  $\theta_{rms}$  is proportional to  $OPD_{rms}$  divided by a characteristic length scale. For the case of a turbulent boundary layer, the relevant length scale is the boundary-layer thickness  $\delta$ . Using Eq. (6) for  $OPD_{rms}$ , the scaling for the deflection angle for the boundary layer becomes

$$\theta_{rms} \sim \frac{OPD_{rms}}{\delta} = F(M_\infty) K_{GD} \rho_\infty M_\infty^2 (C_f)^{1/2} \quad (11)$$

This scaling can also be used to normalize the global streamwise tilt,  $\theta_{G,rms}$  (Aperture). Since the experimental value of  $F(M_\infty)$

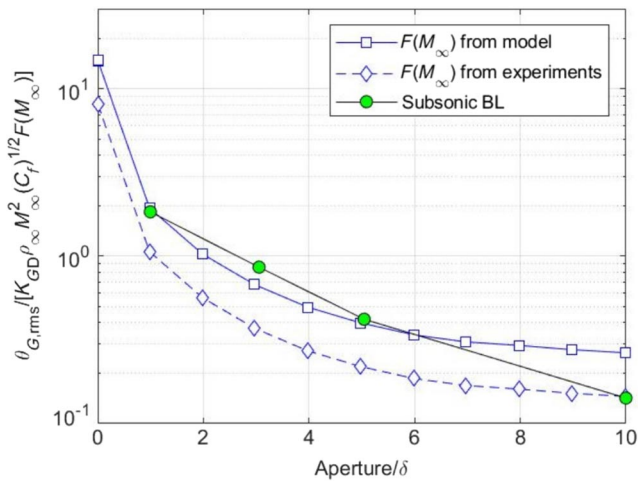


**Fig 13** Normalized levels of the streamwise global jitter,  $\theta_{G,rms}$ , for different apertures, reconstructed from the stitched wavefronts. Global jitter values for the subsonic boundary layer from [25] are also shown for comparison.

deviates from the model prediction (see Fig. 12), both the experimental and the model-predicted values of  $F(M_\infty)$  were used to normalize the global jitter levels. The results are shown in Fig. 13. The levels of the normalized global jitter monotonically decrease with the increased aperture size. Additionally, the model overpredicts the jitter by an approximately constant factor. This is consistent with the deviation observed between the model and experimental  $OPD_{rms}$  results in Fig. 12. In [15] it was derived that the aperture works as a spatial low-pass filter, so the contribution to the global jitter from higher-wavenumber wavefront modes is suppressed for larger apertures, resulting in smaller levels of the global jitter. The normalized global jitter from the subsonic boundary layer [25] is also shown in Fig. 13 for comparison. While trends are similar, the global jitter for the hypersonic boundary layers appears to be 2–3 times smaller in amplitude, compared to the subsonic case. These results can be used to estimate the global streamwise jitter, caused by high supersonic and hypersonic boundary layers, for various aperture sizes.

## V. Conclusions

Aero-optical measurements of turbulent boundary layers on the wall of a Mach 8 wind tunnel were conducted using a double-pass Shack–Hartmann wavefront sensor. Deflection angles were recorded at different sampling rates and spatial resolutions, ranging from a 2-D array sampled at 76 kHz to 1-D slices at 1.75 MHz. A novel de-aliasing algorithm, based on the 2-D Fourier transform, was proposed to isolate the convective-only component of the deflection angle spectra. The de-aliased deflection angle spectra were used to compute the convective speeds of the aero-optical structures and the resulting optical distortion. Two-dimensional wavefronts were processed using a stitching method, providing a complimentary estimate of the level of aero-optical distortions and additional information on the size of the aero-optically active coherent structures. The stitching method was shown to provide estimates of global jitter unbiased from facility vibration. Comparison of the deflection-angle spectra with those at lower Mach numbers showed that the spectral properties of the underlying aero-optical structures do not significantly vary over a wide range of Mach numbers, with a consistent peak at a scale approximately equal to the boundary-layer thickness. Comparison of the measured optical distortion with an existing theoretical model revealed that the experimental results are higher than the model prediction by almost a factor of two at the reported Mach number. The aero-optical component of the global jitter in the streamwise direction was also calculated from the stitched wavefronts. It was demonstrated that the levels of the global jitter, imposed on the outgoing beam, becomes smaller for larger apertures. It was found that the

global jitter is on the same order of magnitude, compared to the global jitter for the subsonic boundary layer. The presented results can be used to estimate aero-optical effects of turbulent boundary layers at high supersonic and hypersonic speeds and to validate numerical simulations of aero-optical distortions at these speeds.

## Acknowledgments

The authors gratefully acknowledge the support of the Laboratory Directed Research and Development program at Sandia National Laboratories. This paper describes objective technical results and analysis. Any subjective views or opinions that might be expressed in the paper do not necessarily represent the views of the U.S. Department of Energy or the United States Government. Sandia National Laboratories is a multimission laboratory managed and operated by National Technology & Engineering Solutions of Sandia, LLC, a wholly owned subsidiary of Honeywell International, Inc., for the U.S. Department of Energy's National Nuclear Security Administration under contract DE-NA0003525.

## References

- [1] Gardiner, W. C., Jr., Hidaka, Y., and Tanzawa, T., "Refractivity of Combustion Gases," *Combustion Flame*, Vol. 40, 1980, pp. 213–219. [https://doi.org/10.1016/0010-2180\(81\)90124-3](https://doi.org/10.1016/0010-2180(81)90124-3)
- [2] Jumper, E. J., and Gordeyev, S., "Physics and Measurement of Aero-Optical Effects: Past and Present," *Annual Review of Fluid Mechanics*, Vol. 49, No. 1, 2017, pp. 419–441. <https://doi.org/10.1146/annurev-fluid-010816-060315>
- [3] Tyson, R. K., *Principles of Adaptive Optics*, Academic Press, New York, 1997, Chap. 6.
- [4] Wang, M., Mani, A., and Gordeyev, S., "Physics and Computation of Aero-Optics," *Annual Review of Fluid Mechanics*, Vol. 44, No. 1, 2012, pp. 299–321. <https://doi.org/10.1146/annurev-fluid-120710-101152>
- [5] Wyckham, C., and Smits, A., "Aero-Optic Distortion in Transonic and Hypersonic Turbulent Boundary Layers," *AIAA Journal*, Vol. 47, No. 9, 2009, pp. 2158–2168. <https://doi.org/10.2514/1.41453>
- [6] Gordeyev, S., Smith, A., Cress, J., and Jumper, E., "Experimental Studies of Aero-Optical Properties of Subsonic Turbulent Boundary Layers," *Journal of Fluid Mechanics*, Vol. 740, 2014, pp. 214–253. <https://doi.org/10.1017/jfm.2013.658>
- [7] Gordeyev, S., Cress, J. A., Smith, A., and Jumper, E. J., "Aero-Optical Measurements in a Subsonic, Turbulent Boundary Layer with Non-Adiabatic Walls," *Physics of Fluids*, Vol. 27, No. 4, 2015, pp. 1–17. <https://doi.org/10.1063/1.4919331>
- [8] Gordeyev, S., Rennie, R. M., Cain, A. B., and Hayden, T. E., "Aero-Optical Measurements of High-Mach Supersonic Boundary Layers," *46th AIAA Plasmadynamics and Lasers Conference*, AIAA Paper 2015-3246, 2015. <https://doi.org/10.2514/6.2015-3246>
- [9] Gordeyev, S., and Juliano, T., "Optical Characterization of Nozzle-Wall Mach-6 Boundary Layers," *54th AIAA Aerospace Sciences Meeting*, AIAA Paper 2016-1586, 2016. <https://doi.org/10.2514/6.2016-1586>
- [10] Gordeyev, S., and Juliano, T., "Optical Measurements of Transitional Events in a Mach-6 Boundary Layer," *AIAA Journal*, Vol. 55, No. 11, 2017, pp. 3629–3639. <https://doi.org/10.2514/1.J055759>
- [11] Winter, M., Green, R., Borchetta, C., Josyula, E., Hayes, J., Jewell, J., and Hagen, B., "Experimental Investigation of Image Distortion in a Mach 6 Hypersonic Flow," *2018 Aerodynamic Measurement Technology and Ground Testing Conference*, 2018. <https://doi.org/10.2514/6.2020-1971>
- [12] Lee, S., Jeong, M., Jeung, I., Lee, H. J., and Lee, J. K., "Aero-Optical Measurement in Shock Wave of Hypersonic Flow Field," *30th International Symposium on Shock Waves*, 2017. [https://doi.org/10.1007/978-3-319-46213-4\\_37](https://doi.org/10.1007/978-3-319-46213-4_37)
- [13] Casper, K. M., Beresh, S., Henfling, J., Spillers, R., Pruett, B., and Schneider, S., "Hypersonic Wind-Tunnel Measurements of Boundary-Layer Pressure Fluctuations," *AIAA Fluid Dynamics Conference*, AIAA Paper 2009-4054, 2009. <https://doi.org/10.2514/6.2009-4054>
- [14] Smith, J. A., DeChant, L. J., Casper, K. M., Mesh, M., and Field, R. V., Jr., "Comparison of a Turbulent Boundary Layer Pressure Fluctuation Model to Hypersonic Cone Measurements," *34th AIAA Applied*

- Aerodynamics Conference*, AIAA Paper 2016-4047, 2016.  
<https://doi.org/10.2514/6.2016-4047>
- [15] Southwell, W. H., "Wave-Front Estimation from Wave-Front Slope Measurements," *Journal of the Optical Society of America*, Vol. 70, No. 8, 1980, pp. 998–1006.  
<https://doi.org/10.1364/JOSA.70.000998>
- [16] Siegenthaler, J., Gordeyev, S., and Jumper, E., "Shear Layers and Aperture Effects for Aero-Optics," AIAA Paper 2005-4772, 2005.  
<https://doi.org/10.2514/6.2005-4772>
- [17] Kemnetz, M. R., and Gordeyev, S., "Analysis of Aero-Optical Jitter in Convective Turbulent Flows Using Stitching Method," *AIAA Journal*, Vol. 60, No. 1, 2022, pp. 14–30.  
<https://doi.org/10.2514/1.J060756>
- [18] Kemnetz, M. R., and Gordeyev, S., "Optical Investigation of Large-Scale Boundary-Layer Structures," AIAA Paper 2016-1460, 2016.  
<https://doi.org/10.2514/6.2016-1460>
- [19] Gordeyev, S., and Kalensky, M., "Effects of Engine Acoustic Waves On Aero-Optical Environment In Subsonic Flight," *AIAA Journal*, Vol. 58, No. 12, 2020, pp. 5306–5317.  
<https://doi.org/10.2514/1.J059484>
- [20] Bendat, J. S., and Piersol, A. G., *Random Data*, Wiley, Hoboken, NJ, 2011, Chap. 11.2.
- [21] Sontag, J., and Gordeyev, S., "Optical Diagnostics of Spanwise-Uniform Flows," *AIAA Journal*, Vol. 60, No. 9, 2022, pp. 1–15.  
<https://doi.org/10.2514/1.J061692>
- [22] Del Álamo, J. C., and Jiménez, J., "Estimation of Turbulent Convection Velocities and Corrections to Taylor's Approximation," *Journal of Fluid Mechanics*, Vol. 640, 2009, pp. 5–26.  
<https://doi.org/10.1017/S0022112009991029>
- [23] Wang, K., and Wang, M., "Aero-Optics of Subsonic Turbulent Boundary Layers," *Journal of Fluid Mechanics*, Vol. 696, 2012, pp. 122–151.  
<https://doi.org/10.1017/jfm.2012.11>
- [24] Korte, J., and Lafferty, J. F., "Determination of Hypervelocity Free-stream Conditions for a Vibrationally Frozen Nitrogen Flow," *AIAA SciTech 2021 Forum*, AIAA Paper 2021-0981, 2021.  
<https://doi.org/10.2514/6.2021-0981>
- [25] Miller, N. E., Guildenbecher, D. R., and Lynch, K. P., "Aero-Optical Distortions of Turbulent Boundary Layers: DNS up to Mach 8," *AIAA Aviation 2021*, AIAA Paper 2021-2832, 2021.  
<https://doi.org/10.2514/6.2021-2832>
- [26] Tyson, R. K., and Frazier, B. W., *Field Guide to Adaptive Optics*, 2nd ed., SPIE Press, Bellingham, WA, 2012, p. 20.

T. I. Shih  
 Associate Editor